

Descattering and Density Reconstruction in Polyenergetic Tomography using Locally-Learned Models

Michael T. McCann, Marc L. Klasky, Jennifer L. Schei, and Saiprasad Ravishankar, *Senior Member, IEEE*

Abstract—We present a method for descattering and quantitative density reconstruction in polyenergetic X-ray computed tomography (CT) based on fitting local models of scatter. X-ray CT is widely used in medical and industrial applications. If not accounted for during reconstruction, X-ray scatter creates a loss of contrast and introduces severe image artifacts including cupping, shading, and streaks. Even when these qualitative artifacts are not apparent, scatter poses a major obstacle in obtaining accurate quantitative radiographic reconstructions. Our approach to estimating scatter is to generate a training set of radiographs with and without scatter using particle transport simulation software. We then learn a locally adaptive model, i.e., one comprised of many models, each fit to a local neighborhood of the training data. We use this scatter model inside an iterative descattering algorithm and reconstruct densities from the corrected data. Our experiments on monoenergetic and polyenergetic data show that, when applied locally, even simple, linear models are highly effective at estimating scatter. Further, descattering approaches based on these local models can reduce the effect of scatter on density reconstruction by more than half.

Index Terms—Inverse problems, tomography, scatter removal, efficient algorithms, optimization, machine learning, deep learning.

I. INTRODUCTION

X-ray computed tomography is used in a variety of medical, industrial, and scientific applications. Typically, attenuation maps of the underlying object are reconstructed in CT from sinogram measurements using techniques such as filtered backprojection or model-based iterative reconstruction (MBIR) [1]. These approaches often assume simple imaging forward models to perform reconstruction.

In this work, our objective is to reconstruct the density field of an object (with known material composition) from radiographs obtained with a polyenergetic X-ray beam. Our focus on quantitative material density reconstruction is somewhat different than in medical physics applications, where the material composition of the object being imaged (and therefore the physical properties that would allow mapping linear

attenuation to density) are unknown and therefore only the linear attenuation map is reconstructed, (with some exceptions, e.g., [2]). The application of a polyenergetic beam introduces another complication to our problem as compared to medical imaging, where often (although not always, e.g., [3]) a monoenergetic source is assumed. In our setting, we assume known materials, which gives us the opportunity to reconstruct density without facing an under-determined problem.

X-ray scatter poses a major obstacle in obtaining quantitative radiographic reconstructions. In general, scatter creates loss of contrast impairing the ability to find sharp features as well as introducing severe image artifacts, e.g., cupping, shading, streaks, etc. Consequently, in applications in which a quantitative density reconstruction is desired, scatter must be either removed via preprocessing or accounted for during reconstruction; tomographic reconstruction algorithms such as FBP or MBIR typically ignore the effect of scatter. Scatter is a complex phenomenon in which the individual radiation/matter interactions (as X-ray photons pass through an object) may be described by physical laws, e.g., Klein Nishina for Compton scattering, bremsstrahlung, coherent scatter, pair production, and photoelectric effect [4]. The individual scattering interactions may each be represented by convolutions, where the magnitude of the scatter produced for single interactions is proportional to the probability of interaction, i.e., areal mass along the direction of each ray. However, the difficulty in even representing single scattering events with convolutions is that the transport of the scattered radiation is in a direction away from the direction of the initial scattering interaction. Consequently, the resulting scatter that contributes to form the image is a function of the magnitude of the scattered radiation produced, its angular distribution and the density distribution of the object. This motivates a model in which a convolutional kernel is utilized to capture the spatial aspects of scatter, but where the kernel somehow changes in response to the density distribution of the object.

We propose a new scatter estimation/correction and density reconstruction algorithm based on learning local models from a dataset of scatter simulations. In this approach, a training dataset of paired radiographs—with and without scatter—is used at during reconstruction to learn a local scatter model, which makes the approach scan-adaptive. We compare the local approach to a more conventional global fitting approach—where a single model is fit on the entire training set prior to reconstruction—using four types of models, including two from the recent descattering literature [5]. In an experiment

M. T. McCann is with the Department of Computational Mathematics, Science and Engineering at Michigan State University, East Lansing, MI, 48824 USA (email: mccann13@msu.edu).

M. L. Klasky and J. L. Schei are with the Physics Division at Los Alamos National Laboratory, Los Alamos, NM, 87545 USA.

S. Ravishankar is with the Department of Computational Mathematics, Science and Engineering and the Department of Biomedical Engineering at Michigan State University, East Lansing, MI, 48824 USA (email: ravisha3@msu.edu).

with simulated monoenergetic radiographs, we show that local descattering is sufficient to almost completely remove the scatter, reducing median density errors from 0.656 g/cm^3 to under 0.05 g/cm^3 . In a more challenging polyenergetic simulation experiment, we were able to reduce median density error from 0.550 g/cm^3 to under 0.25 g/cm^3 . Based on our experiments, we conclude that a simple, convolutional model of scatter provides excellent descattering and quantitative density reconstruction when it is fit in the proposed local manner.

A. Related Work in Scatter Correction

There exists a vast literature on scatter correction, beginning in at least 1976 [6] and presented in the context of many different scanners and applications, from keV CT for medical imaging to MeV CT for nondestructive testing (where keV and MeV refer to the nominal energy of the X-ray photons). Here, we aim to discuss the main trends in computational approaches to scatter correction, see the pair of reviews [7], [8] for more comprehensive coverage.

Most scatter correction techniques rely on scatter estimation, and can therefore be classified by what information they estimate the scatter from, e.g., the total transmission radiograph, a descattered radiograph, or the reconstructed density [7]. Scatter estimation from a reconstructed density can be highly accurate, because, in principle, the density fully determines the scatter. In practice, it is slow because it necessitates alternating between approximate reconstruction of the 3D density and scatter estimation and removal. Scatter estimation from the total transmission (i.e., the radiographic measurements corrupted by scatter) has the advantage of providing single-shot descattering: no iteration is required; however, these methods have limited accuracy because some approximation is involved when predicting scatter without access to the underlying density. Scatter estimation from a descattered radiograph strikes a balance between accuracy and speed, requiring only iteration in the radiograph domain (the scatter is repeatedly estimated and removed based on iteratively estimated clean radiographs) thereby avoiding the need to perform multiple high-dimensional density reconstructions. Which scatter estimation approach is best depends on the application: the amount and dominant mechanism of scatter, the requirements on descattering and reconstruction time, and the desired accuracy of the reconstructions.

In this work, our focus is on iterative scatter estimation from the descattered radiograph; most methods in this class use some form of the model

$$s[m, n] = \sum_{m', n'} f(\mathbf{d}[m', n']) \mathbf{H}_\rho[m', n', m, n], \quad (1)$$

where $s[m, n]$ and $\mathbf{d}[m, n]$ are the scatter (only) and direct (without scatter) radiographs at position m, n and f is a scalar function. The term $f(\mathbf{d}[m, n])$, sometimes called the *scatter potential* or *scatter amplitude factor*, represents how much scatter comes off of a given pixel. The term $\mathbf{H}_\rho[m', n', m, n]$, called the *scatter kernel*, represents how much radiation scatters from position m', n' to position (m, n) . In the most

general case, it is dependent on the 3D density field of the object being imaged, ρ .

The model (1) is hardly useful as it is because it is so general. The challenge is simplifying it to a point where it can be parameterized and the parameters estimated. One common approach is to fix the scatter amplitude factor to the parametric form $f(x) = x^\alpha |\ln x|^\beta$, which can be motivated by a simple physical model [9]. Another is to constrain the scatter kernel to be shift invariant, $\mathbf{H}_\rho[m', n', m, n] = \mathbf{H}_\rho[m' - m, n' - n]$, or a spatially-varying weighted sum of such kernels, where the weights may depend on (estimated) object thickness or distance to the object boundary [5]. There also exists recent work that uses a convolutional neural network to map from a direct radiograph to the corresponding scatter radiograph [10], which we can view as an overparameterized and nonlinear version of (1).

No matter the form of the scatter model, its parameters must be determined in order to perform scatter estimation. One approach is to fit the parameters on simple simulations, e.g., of a pencil beam through a slab [5], [11]. Another is to approach fitting as an optimization problem on complex reference simulation(s) [10]. The benefit of the former approach is that it may generalize well and fits well with physically interpretable models. The benefit of the latter is that it may provide more accurate fits, because it explicitly minimizes fit error.

B. Contributions and Outline

Our main contribution is to propose a locally learned model of scatter, wherein the free parameters of a given model are fit on training data in a local neighborhood around the radiograph to be descattered. We emphasize that the proposed model is local in the sense that the model changes as a function of the input—as distinct from spatially local models, where the model changes as a function of location in the radiograph. The advantage of the proposed method, is that, when fit locally, even simple models can describe scatter well, thus avoiding the algorithmic challenges and computational burden of fitting and using a nonlinear or shift-variant model. Figure 1 gives an overview of the approach.

The rest of the manuscript is organized as follows. In Section II, we discuss the descattering problem, including the forward model for monoenergetic and polyenergetic tomography. In Section III, we discuss local modeling in general, then describe local models for scatter estimation and our descattering algorithm. In Section V, we present experiments validating our proposed local modeling approach. We provide additional discussion in Section VI and conclude in Section VII.

II. MONOENERGETIC AND POLYENERGETIC TOMOGRAPHY WITH SCATTER

The overall goal of this work is to recover a discretized, space-varying density $\rho \in \mathbb{R}^{N_1 \times N_2 \times N_3}$, from a set of V tomographic measurements (also called radiographs), $\{\mathbf{t}_v\}_{v=1}^V$, $\mathbf{t}_v \in \mathbb{R}^{M_1 \times M_2}$, where v indexes the viewing direction. In this section, we describe the forward model that relates ρ

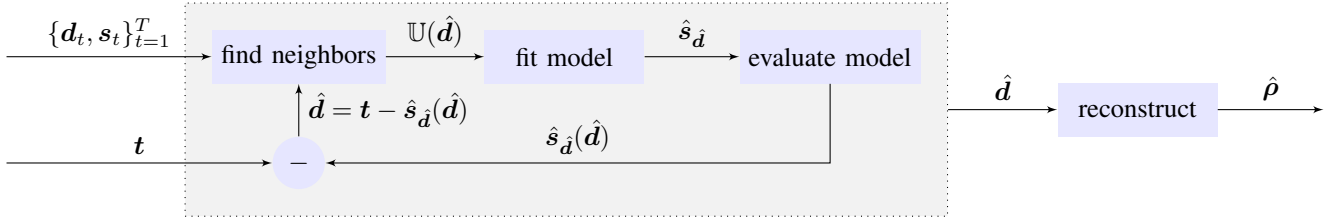


Fig. 1: Block diagram of the proposed local descattering and reconstruction scheme, which reconstructs a density field, $\hat{\rho}$, from a total transmission radiograph, t , and a training set, $\{d_t, s_t\}_{t=1}^T$. The shaded region corresponds to Algorithm 1; details are given in Sections III and IV.

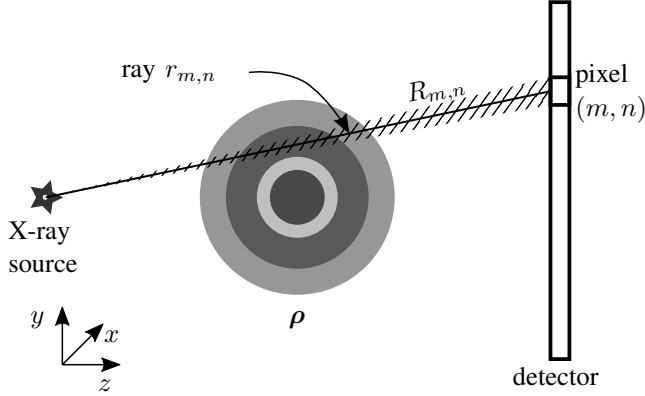


Fig. 2: Sketch of the tomography setup. In reality, the object is 3D and the detector is a plane. $\rho \in \mathbb{R}^{N_1 \times N_2 \times N_3}$ denotes the density field of the object being imaged, $R_{m,n}$ is the set of rays entering detector pixel (m, n) , and $r_{m,n}$ is the central ray of $R_{m,n}$.

to $\{t_v\}_{v=1}^V$; much of our presentation is adapted from the standard textbook [12].

In a generic radiographic setup (see Figure 2 for a sketch), there is an X-ray source, one or more objects being imaged, and a detector. Every ray between the source and detector, r , intersects a certain amount of each object. This is called the areal density of the object along r ,

$$\rho_{A_i}(r) = \int_{-\infty}^{\infty} \rho_i(r_x(t), r_y(t), r_z(t)) dt, \quad (2)$$

where $\rho_{A_i}(r)$ has units g/cm^2 , $r_x(t), r_y(t), r_z(t)$ are a parameterization of the ray r , and i is the object index—each different material being imaged corresponds to a different i . We note a slight abuse of notation here: a continuous ρ in (2) versus a discrete ρ mentioned before; we will put aside the details of discretization here as they are an implementation detail of the reconstruction software discussed in Section IV.

A. Monoenergetic Case

In the absence of scatter and with a monoenergetic source, the number density of photons reaching the detector along ray r is

$$q(r) = q_{\text{in}}(r) \exp\left(-\sum_i \xi_i \rho_{A_i}(r)\right), \quad (3)$$

where $q(r)$ has units $1/\text{cm}^2$, $q_{\text{in}}(r)$ is the number density of the incident beam along ray r , and $\xi_i \in \mathbb{R}$ is the mass attenuation coefficient of the i th material, with units cm^2/g . In our application, we assume known materials, therefore the mass attenuation coefficients can be looked up, e.g., in the XCOM database [13].

In reality, what we measure is not the number density of photons at infinitesimal points, as given by (3), but a discrete, finite image which represents the number of photons reaching each of a finite grid of detectors. We refer to this scatter-free measurement data as the direct radiograph, $d \in \mathbb{R}^{M_1 \times M_2}$. It is given by

$$d[m, n] = \int_{R_{m,n}} q(r) dr \approx q(r_{m,n}) \Delta x^2 \quad (4)$$

where $d[m, n]$ is unitless, $R_{m,n}$ is the set of rays entering detector pixel (m, n) , $r_{m,n}$ is the ray through the center of pixel (m, n) , and Δx^2 gives the area of a detector pixel; the approximation holds when the detector elements are sufficiently small and regular in size (think pixels). Real measurement systems also have a per-pixel gain, meaning that we actually measure $c[m, n]d[m, n]$. We ignore this gain factor as it is easily handled via calibration.

B. Polyenergetic Case

In the polyenergetic case, we have

$$q(r) = \int_0^{\infty} q_{\text{in}}(r, E) \exp\left(-\sum_i \xi_i(E) \rho_{A_i}(r)\right) dE, \quad (5)$$

where $q_{\text{in}}(r, E)$ is the energy profile of the number density of the incident beam and $\xi_i(E)$ gives the mass attenuation coefficient of the i th material at energy E . Using the same numerical integration approximation as in the monoenergetic case and an additional quadrature for energy gives

$$d[m, n] \approx \sum_e q(r_{m,n}, E_e) \Delta x^2 \Delta E, \quad (6)$$

where e indexes discrete energy bins, ΔE is the energy bin width, and

$$q(r, E) = q_{\text{in}}(r, E) \exp\left(-\sum_i \xi_i(E) \rho_{A_i}(r)\right). \quad (7)$$

In some cases, it is sufficient to stop at the model for the direct radiograph given by (4) or (6). However, in many cases, there is a nontrivial amount of scatter, i.e., photons

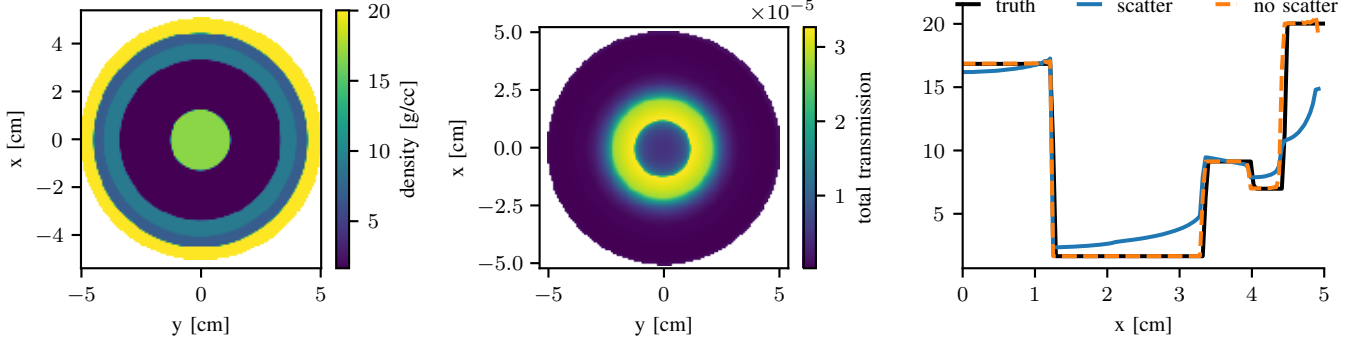


Fig. 3: Illustration of how the presence of scatter negatively impacts quantitative density reconstruction (monoenergetic dataset). Left: Cross section showing the density of a spherically symmetric, 3D object. Center: Radiographic measurement of the object on the left, which includes scatter. Our goal is to reconstruct the left image from the center one. Right: 1D profiles of the true density and reconstruction from radiographs with and without scatter. Without scatter, reconstruction is nearly perfect (orange, dotted line overlaps black); with scatter, reconstruction involves density errors on the order of 1 g/cm³.

that reach the detector without following a straight path through the object (Figure 3 illustrates the effect this scatter on reconstruction). Scatter arises from several different physical processes. A photon may

- undergo exactly one coherent scattering interaction with the object;
- undergo exactly one Compton scattering interaction with the object;
- interact with and scatter from the scene, i.e., parts of the measurement apparatus other than the object we want to image; or
- undergo any other interaction(s) not included above, e.g., multiple scatters or pair production.

These processes are well understood, but they are complicated enough that they need to be modeled at the individual photon level, a computationally expensive process and one that is difficult to invert. For our purposes, we consider the measured radiograph $\mathbf{t} \in \mathbb{R}^{M_1 \times M_2}$ as a sum of direct photons, \mathbf{d} as described in (4) or (6), and scattered photons, $\mathbf{s} \in \mathbb{R}^{M_1 \times M_2}$,

$$\mathbf{t}[m, n] = \mathbf{d}[m, n] + \mathbf{s}[m, n]. \quad (8)$$

We will also refer to \mathbf{t} as the total radiograph, since it contains both the contribution of the scattered and direct photons. Finding a way to efficiently and accurately model \mathbf{s} is the main focus of this work.

III. PROPOSED APPROACH—LOCAL LEARNING FOR DESCATTERING

As stated earlier, the goal of this work is to recover the object, ρ , from its tomographic measurements $\{\mathbf{t}_v\}_{v=1}^V$. Our proposed approach consists of two steps: descattering and reconstruction; we now discuss the first of these.

We begin by introducing our proposed local modeling approach in general, and then in the context of scatter estimation. We finish with a description of our descattering algorithm.

A. Local Modeling in Image Reconstruction

Consider an image reconstruction problem,

$$\operatorname{argmin}_{\mathbf{x}} \|\mathcal{A}\{\mathbf{x}\} - \mathbf{y}\|, \quad (9)$$

where $\mathbf{x} \in \mathbb{R}^N$ is a (vectorized) image, $\mathbf{y} \in \mathbb{R}^M$ are measurements, and $\mathcal{A} : \mathbb{R}^N \rightarrow \mathbb{R}^M$ is a nonlinear and computationally expensive forward model. (The norm or other discrepancy functional in (9) may depend in practice on measurement statistics.) In a typical iterative scheme for solving (9), we would need to compute tens or hundreds of gradients of \mathcal{A} with respect to \mathbf{x} , which means reconstruction will be intolerably slow.

Our proposed approach is to approximate \mathcal{A} via a large number of simple, local models, i.e., a collection of $\hat{\mathcal{A}}_{\mathbf{x}}$'s, each acting in a different region of \mathbb{R}^N . First, we generate a fixed training set, $\{(\mathbf{x}_t, \mathcal{A}\{\mathbf{x}_t\})\}_{t=1}^T$, where the \mathbf{x}_t 's are chosen to represent the variety of objects we might want to reconstruct. Next, we fix a (problem-specific) distance D (e.g., the Euclidean norm, Wasserstein metric, etc.) and define the nearest neighbor function, $\mathbb{U}(\mathbf{x})$, to return the set of indices of the G nearest training pairs to \mathbf{x} in the training set, i.e.,

$$\mathbb{U}(\mathbf{x}) = \{t_1, t_2, \dots, t_G\}, \quad (10)$$

such that $D(\mathbf{x}, \mathbf{x}_s) \leq D(\mathbf{x}, \mathbf{x}_t)$ for $s \in \mathbb{U}(\mathbf{x})$ and $t \notin \mathbb{U}(\mathbf{x})$. Finally, we select a class, \mathcal{H} , of models for the local $\hat{\mathcal{A}}_{\mathbf{x}}$'s, e.g., linear, constant, convolutional, parametric nonlinear, etc.

Our model for \mathcal{A} is then given by

$$\hat{\mathcal{A}}\{\mathbf{x}\} = \hat{\mathcal{A}}_{\mathbf{x}}\{\mathbf{x}\}, \quad (11)$$

where

$$\hat{\mathcal{A}}_{\mathbf{x}} = \operatorname{argmin}_{\hat{\mathcal{B}} \in \mathcal{H}} \sum_{t \in \mathbb{U}(\mathbf{x})} \|\hat{\mathcal{B}}\{\mathbf{x}_t\} - \mathcal{A}\{\mathbf{x}_t\}\|. \quad (12)$$

Put simply: to predict $\mathcal{A}\{\mathbf{x}\}$, we fit a model on the nearest neighbors to \mathbf{x} in the training set and apply that model to \mathbf{x} . For this approach to be advantageous, it requires both that the time it takes to solve (12) and apply $\hat{\mathcal{A}}_{\mathbf{x}}$ is less than the time

it takes to apply \mathcal{A} and that \mathcal{A} is sufficiently well-modeled by the $\hat{\mathcal{A}}_x$'s.

Before moving on, we make a few brief comments. First, our presentation assumes that \mathcal{A} is known and computable, albeit slowly. In a real image reconstruction problem, there is a true underlying forward model that can never be perfectly known; we are not addressing the issue of learning that model here. Second, we have motivated local learning from an inverse problem perspective because it fits our application here, but the approach is completely general: any image-to-image function can be approximated this way, whether it represents some physical forward model or not. For example, the same approach could be used to approximate an inverse of \mathcal{A} , simply by exchanging the role of \mathbf{x}_t and $\mathcal{A}\{\mathbf{x}_t\}$. Finally, the local learning can efficiently handle changes in the training data set at deployment time (e.g., addition of new samples or removal of samples), without expensive retraining.

B. Local and Global Models of Scatter

We now discuss local modeling as it applies to the descattering problem. The aim of the descattering algorithm is to recover an estimate of the direct signal, \mathbf{d} , from a corresponding total signal, \mathbf{t} . To do this, we attempt to model the corresponding scatter, \mathbf{s} , as a function of \mathbf{d} and solve

$$\mathbf{t} = \hat{\mathbf{s}}(\mathbf{d}) + \mathbf{d} \quad (13)$$

for \mathbf{d} . (One could readily incorporate regularization on \mathbf{d} and terms modeling noise or other errors in this model; we leave these for future work.)

To specify this scatter model, we use a training set consisting of direct and scatter pairs, $\{(\mathbf{d}_t, \mathbf{s}_t)\}_{t=1}^T$. These training radiographs can be formed by generating synthetic objects, ρ_t , and simulating their radiographs via particle transport software, e.g., MCNP [14] or Geant4 [15]¹. We discuss the details of our training set generation in Section V-A.

We propose a scatter model that adapts at testing time by fitting a model to subsets of the training set, as described in the previous section. In our experiments, we compare four classes of local models. The first two (single field and free kernel) are simple models that we propose; the second two (parametric and multikernel) come from the scatter modeling literature [5].

The **single field model** represents the scatter as being a constant field, i.e., $\hat{\mathbf{s}}_{\mathbf{d}}(\mathbf{d}) = \hat{\mathbf{s}}_{\mathbf{d}} \in \mathbb{R}^{M_1 \times M_2}$. Fitting the single field model requires solving the problem

$$\hat{\mathbf{s}}_{\mathbf{d}} = \operatorname{argmin}_{\mathbf{s} \in \mathbb{R}^{M_1 \times M_2}} \sum_{t \in \mathbb{X}} \|\mathbf{s} - \mathbf{s}_t\|_F^2, \quad (14)$$

where \mathbb{X} may represent either the entire training set (*global fitting*) or $\mathbb{U}(\mathbf{d})$ (*local fitting*). Note the use of a subscript \mathbf{d} : $\hat{\mathbf{s}}_{\mathbf{d}}$ is a model (i.e., an image-to-image function) fit on the neighbors of \mathbf{d} ; $\hat{\mathbf{s}}_{\mathbf{d}}(\mathbf{d})$ is that model evaluated at the point \mathbf{d} , which is an image. The solution to (14) is easily obtained by taking the pixelwise average of the $\{\mathbf{s}_t\}_{t \in \mathbb{X}}$. In the case

where one neighbor is used, i.e., $G = 1$ in (10), the single field model is the classical nearest neighbor interpolator.

The **free kernel model** represents the scatter as a convolution. The form of the model is $\hat{\mathbf{s}}(\mathbf{d}) = \mathbf{k}_{\mathbf{d}} * \mathbf{d}$. Here, $\mathbf{k}_{\mathbf{d}} * \mathbf{d}$ denotes the linear convolution between zero-padded versions of $\mathbf{k}_{\mathbf{d}}$ and \mathbf{d} , where the result is cropped to match the support of \mathbf{d} . The size of the kernel is the smallest such that each point in \mathbf{d} can contribute to each point in $\mathbf{k}_{\mathbf{d}} * \mathbf{d}$, thus $\mathbf{k}_{\mathbf{d}} \in \mathbb{R}^{(2M_1-1) \times (2M_2-1)}$.

We fit the kernel by solving the optimization problem

$$\mathbf{k}_{\mathbf{d}} = \operatorname{argmin}_{\mathbf{k}} \sum_{t \in \mathbb{X}} \|\mathbf{k} * \mathbf{d}_t - \mathbf{s}_t\|_F^2 \quad \text{s.t.} \quad \mathbf{k} \geq \mathbf{0}, \quad (15)$$

where, \mathbb{X} is an appropriate set of training indices, $\|\cdot\|_F^2$ denotes the squared Frobenius norm (sum of the squared elements), and the constraint should be interpreted elementwise. The nonnegativity constraint ensures that scatter estimates from this model can never be negative, which makes physical sense.

The problem (15) boils down to a nonnegative least squares problem—a well-studied topic, see, e.g., the survey [16]. The main challenge here is that, while $\mathbf{k} * \mathbf{d}$ is a linear operation on \mathbf{k} and can therefore be written as $\mathbf{D}\mathbf{k}$, the corresponding matrix \mathbf{D} would be $M_1 M_2 \times (M_1 - 1)(M_2 - 1)$, which is too large to store in memory for even medium-sized images (e.g., $256^2 \times 511^2 \times 8$ bytes ≈ 137 gigabytes). As a result, we are restricted to *matrix-free* methods for solving (15), i.e., those that do not involve factoring this large matrix. While there are methods specifically designed for nonnegative least squares, e.g., [17], we use the ADMM method [18] (equations 3.5-3.7). Specifically, we apply ADMM to (15) after introducing the split variable $\mathbf{z} = \mathbf{k}$, so that the quadratic term and nonnegativity constraint separate. The ADMM subproblems are then a quadratic update (which we solve with the conjugate gradient method [19]) and a simple projection onto the positive orthant.

The **parametric kernel model** is a parametric version of the free kernel model with an additional, parametric nonlinearity. It appears in the recent literature on descattering, e.g., [5]. The form of the model is

$$\hat{\mathbf{s}}(\mathbf{d}) = -\mathbf{k}_{A,B,\sigma_1,\sigma_2} * (\mathbf{d}^\alpha (\log \mathbf{d})^\beta), \quad (16)$$

where the log and powers are taken elementwise. To make sense of the negative sign before the log, note that, by convention, \mathbf{d} is normalized by a flat field image so as to be less than or equal to one; we discuss this further in Section IV. The kernel \mathbf{k} is a sum of two centered Gaussian functions,

$$\frac{A}{\sigma_1 \sqrt{2\pi}} \exp\left(-\frac{(m-m_0)^2 + (n-n_0)^2}{2\sigma_1^2}\right) + \frac{B}{\sigma_2 \sqrt{2\pi}} \exp\left(-\frac{(m-m_0)^2 + (n-n_0)^2}{2\sigma_2^2}\right). \quad (17)$$

Fitting the parametric kernel model involves the following nonconvex optimization with respect to the scalar parameters $A, B, \sigma_1, \sigma_2, \alpha$, and β ,

$$\operatorname{argmin}_{A,B,\sigma_1,\sigma_2,\alpha,\beta} \sum_{t \in \mathbb{X}} \|\hat{\mathbf{s}}(\mathbf{d}) - \mathbf{s}_t\|_F^2. \quad (18)$$

¹One could imagine doing the same with real objects, but it would be a significant challenge to manufacture a sufficiently large training set.

We solve it using the LBFGS algorithm [20] (using the PyTorch implementation), which we found to be significantly faster than gradient descent.

The **multikernel model**, proposed in [5], is a generalization of the parametric kernel model wherein different parameters are used in different regions of the image. To fit K kernels, $K - 1$ thresholds, $\tau_1, \tau_2, \dots, \tau_{K-1}$ are established and a partition function is defined according to

$$\mathbf{r}_d[m, n] = \begin{cases} 1 & 0 \leq -\log(\mathbf{d}[m, n]) \leq \tau_1 \\ 2 & \tau_1 < -\log(\mathbf{d}[m, n]) \leq \tau_2 \\ \vdots & \vdots \\ K & \tau_{K-1} < -\log(\mathbf{d}[m, n]). \end{cases} \quad (19)$$

The model is then given by

$$\hat{\mathbf{s}}(\mathbf{d}) = \sum_{k=1}^K -\mathbf{k}_{A_k, B_k, \sigma_{1,k}, \sigma_{2,k}} * (\mathbf{1}_{\mathbf{r}_d=k} \odot \mathbf{d}^{\alpha_k} (\log \mathbf{d})^{\beta_k}), \quad (20)$$

where each kernel is given by (17) and the indicator function is given by

$$\mathbf{1}_{\mathbf{r}=k}[m, n] = \begin{cases} 0, & r[m, n] \neq k; \\ 1, & r[m, n] = k, \end{cases} \quad (21)$$

and \odot indicates elementwise multiplication. Put simply, the multikernel model uses a combination of parametric kernel models, each acting in a different region of the input (specified by the indicator). Fitting the multikernel model, like the parametric kernel, involves solving a nonconvex optimization problem over all the scalar parameters, for which we again use the LBFGS algorithm.

C. Descattering Algorithm

We have so far discussed scatter estimation from a known direct radiograph, but our ultimate goal is descattering, estimating a direct radiograph from a total radiograph containing scatter. With the scatter models from Section III-B in hand, we are ready to descatter by solving (13). The proposed data-driven descattering problem is complex and involves additional underlying optimization problems such as (14), (15), or (18) that can themselves be challenging and nonconvex.² We adopt an iterative fixed-point method for solving (13). Fixed-point algorithms are commonly used for descattering, e.g., see [5]. The wrinkle is that, in the local learning case, the scatter model parameters themselves change as a function of the current estimate of \mathbf{d} . The pseudocode for our descattering algorithm is given in Algorithm 1 and we summarize our entire approach in Figure 1.

IV. MONOENERGETIC AND POLYENERGETIC DENSITY RECONSTRUCTION

After descattering, we have an estimate of the set of direct radiographs, $\{\mathbf{d}_v\}_{v=1}^V$, wherein each \mathbf{d}_v is estimated independently. We now describe how we reconstruct the density field of the object, ρ from this set, which amounts to inverting (4)

²When adapting local models and descattering simultaneously, the descattering problem can be viewed in the framework of bilevel optimization.

Algorithm 1 Fixed point descattering.

```

1: function DESCATTER
2:   input:  $\mathbf{t}; \{(\mathbf{d}_t, \mathbf{s}_t)\}_{t=1}^T$ ; no. of iterations
3:   output: estimated direct  $\mathbf{d}$ 
4:   initialize:  $\mathbf{d} \leftarrow \mathbf{t}$ ,
5:   for no. of iterations do
6:     fit a model,  $\hat{\mathbf{s}}_{\mathbf{d}}$       ▷ e.g., via (14), (15), or (18)
7:      $\mathbf{d} \leftarrow \mathbf{t} - \hat{\mathbf{s}}_{\mathbf{d}}(\mathbf{d})$ 
8:      $\mathbf{d}[\mathbf{d} < 0] \leftarrow 0$     ▷ enforces nonnegativity of  $\mathbf{d}$ 
9:   end for
10:  return  $\mathbf{d}$ 
11: end function

```

or (6) (and, consequently, (3) or (5) and (2)) with respect to the underlying density. In general, if the inversion is ill-posed (e.g., limited view imaging), additional regularization can be used during reconstruction [21], [1]. Here, we consider the case when enough views are acquired to adequately reconstruct the 3D object. In particular, because the objects we are imaging are spherically symmetric, a single view suffices for reconstruction [22].

A. Monoenergetic Case

In the monoenergetic, single-material case, the areal density from a given angle, ρ_{A_v} , can be easily recovered from the direct radiograph at that angle, \mathbf{d}_v . Given a flat field image (an image with no object),

$$\mathbf{f}[m, n] \approx q_{\text{in}}(r_{m,n}) \Delta x^2, \quad (22)$$

we have

$$\frac{\mathbf{d}_v[m, n]}{\mathbf{f}[m, n]} = \exp(-\xi \rho_{A_v}(r_{m,n})). \quad (23)$$

Taking the negative logarithm (pixelwise) and dividing by the mass attenuation coefficient gives $\rho_{A_v}(r)$. Going from $\{\rho_{A_v}\}_{v=1}^V$ to ρ is a standard tomography problem that can be resolved by any of numerous direct [12], iterative [23], or learning-based [21], [1] methods. We work with axisymmetric objects in our experiments and therefore use the three-point algorithm of [22] from the PyAbel Python package.

We also consider the monoenergetic, multimaterial case, where there are nuisance objects: elements of the scene that we are not interested in reconstructing. If these can be imaged without the object of interest, their effect can simply be included in the flat field radiograph and divided out as described above. If they cannot be imaged alone, but we know the distribution of their mass, we can compute their linear attenuation map (mass attenuation coefficient multiplied by areal density) and subtract it after taking the log. Barring these types of prior information, the reconstruction problem is much more challenging and beyond the scope of this paper.

B. Polyenergetic Case

In the single-material, polyenergetic case, we propose to follow the same two-step inversion as in the monoenergetic case; however this is challenging because we cannot simply

divide to remove the effect of the incident field q_{in} (due to its dependence on energy) and we cannot use a logarithm to invert the sum of exponentials that appears in (7). To deal with q_{in} , we make the simplifying assumption that it is separable into an (unknown) space-dependant and a (known) energy-dependent term as $q_{\text{in}}(r, E) = q_{\text{in}}(r)q_E(E)$ with $\sum_e q_E(E_e) = 1$. Under this assumption, division by the flat field gives

$$\frac{\mathbf{d}_v[m, n]}{\mathbf{f}[m, n]} = \sum_e q_E(E_e) \exp(-\xi(E_e)\rho_{A_v}(r_{m, n})). \quad (24)$$

Our solution relies on the fact that (24) is a monotone, scalar function of ρ_{A_v} and therefore invertible via a lookup table. Our density reconstruction algorithm is as follows. We consider (24) as a scalar function of areal mass

$$g(\rho_A) = \sum_e q_E(E_e) \exp(-\xi(E_e)\rho_A). \quad (25)$$

We use this expression to compute $g(\rho_{A_0}), g(\rho_{A_1}), \dots, g(\rho_{A_{L-1}})$, for a set of L areal masses spaced evenly between 0 and some $\rho_{A_{L-1}} = \rho_{A_{\text{max}}}$, the largest areal mass we expect to encounter (if necessary, this can be determined iteratively). For each pixel of the direct transmission, we can then perform a lookup in g to find the corresponding ρ_A (e.g., by using the `interp` function in NumPy [24]). Once the $\{\rho_{A_v}\}$ are recovered, reconstructing ρ is a standard tomography problem, exactly like in the monoenergetic case.

In the polyenergetic, multimaterial case, we cannot treat the nuisance objects as part of the flat field and divide them out, nor can we subtract off a known linear attenuation. For a single nuisance object with known density field, e.g., a collimator,

$$g(\rho_A, m, n) = \sum_e q_E(E_e) \exp(-\xi(E_e)\rho_A - \xi_\eta(E_e)\rho_{A_\eta}(r_{m, n})), \quad (26)$$

where $\xi_\eta(E_e)$ and ρ_{A_η} denote the known mass attenuation coefficient and areal mass of the nuisance object. Inverting (26) requires a three dimensional lookup table, which we can interpret as a version of the lookup table for (25) for each location, (m, n) . The same approach can be used for multiple nuisance objects by adding more terms to the exponential in (26).

V. EXPERIMENTS AND RESULTS

To evaluate our algorithms, we performed several descattering and reconstruction experiments with simulated data. In this section, we describe our datasets and present a sequence of experiments: First, we show the effects of uncorrected scatter on density reconstructions. Second, we quantify the ability of each model to fit scatter in the oracle case, i.e., when both the scatter and direct radiographs are known. Third, we quantify scatter fitting from training data, thereby testing the ability of each model to generalize. Finally, we compare the models in the context of descattering and density reconstruction from total transmission radiographs. After these experiments, we present small explorations, one into cases with higher densities (and therefore increased scatter) and another into the effect of the number of neighbors for local models.

A. Datasets

Our experiments used two realistic simulation datasets, one with a monoenergetic X-ray source and one with a polyenergetic X-ray source. We generated synthetic radiographs using MCNP6 [14] that consisted of five concentric shells. The outermost shell had a fixed radius of 5 cm and the other four shell radii were randomly varied between 0.25 and 2.5 cm. The material was set to uranium for the entire object, but the density of each shell was randomly selected from a set of five densities, and the mass of the object was conserved through a multiplicative constant. The object center was placed 133 cm from the source and the detector was placed at 525 cm from the source. A tantalum collimator was placed at 98 cm from the source. While the collimator design was not modified for each object, it served to reduce the dynamic range of the image, in general. The monoenergetic single-material dataset was generated using a 1.5 MeV X-ray source and the polyenergetic single-material dataset was generated using a bremsstrahlung with a 19.4 MeV endpoint energy. Radiographs of direct and scattered radiation were generated separately.

For the monoenergetic dataset, we generated 99 pairs of direct and scatter radiographs. For the polyenergetic dataset, we generated 100 pairs. In both cases, we partition the datasets into a testing set consisting of ten pairs (used for evaluation of algorithms) and a training set consisting of the remaining pairs (used for fitting models).

B. Implementation Details

In all experiments, scatter models were fit as described in Section III-B, and all code was written in Python. The area outside the object, i.e., beyond a 5cm radius, was excluded in all cost functionals. Full-resolution images were 257×257 , but scatter fitting was performed on $4 \times$ downsampled versions and scatter estimations were upsampled to the original size using bilinear interpolation. The entire training set was scaled to unit norm before fitting and the same scaling was applied at testing time. For ADMM, the number of iterations was 20, with 5 CG iterations per iteration, and the penalty parameter was set to 1.0. For both the parametric kernel and multikernel models, the number of LBFGS iterations was 20 with step size 1.0 and back-tracking line search enabled; the initial parameters were $A = 1.0, B = 1.0, \sigma_1 = 4, \sigma_2 = 64, \alpha = 0, \beta = 0$. While we did not make a careful study of the runtimes of the proposed methods, fitting global models was slower than fitting local ones (minutes verses seconds on a consumer-level laptop) and evaluating the models once fit took under a second for all models.

Inverse Abel transforms were performed with the three-point algorithm of [22] from the PyAbel Python package. Polyenergetic reconstructions were slower than monoenergetic ones due to the lookup table, but both took on the order of seconds on a consumer-level laptop.

Code for our method is available upon request.

C. Box and Whisker Plots

Throughout this section, we summarize results using box and whisker plots, e.g., see Figure 4. Unless otherwise noted,

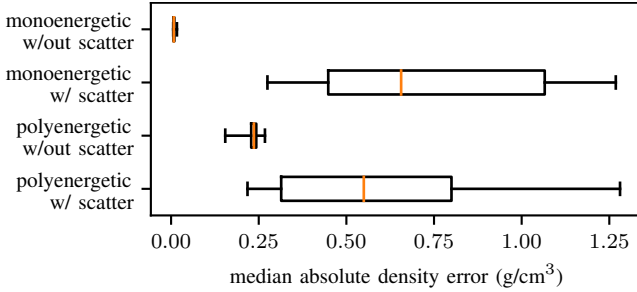


Fig. 4: Accuracy of density reconstruction without and with scatter for the monoenergetic and polyenergetic data test sets. From top to bottom, the median values are 0.008, 0.656, 0.236, and 0.550.

each box summarizes ten testing images. Whiskers indicate minimum and maximum values and boxes indicate first and third quartile. The orange line in the center of each box indicates the median value.

D. Density Reconstruction Without Descattering

Performing density reconstruction from radiographs with and without scatter gives us bounds on the possible performance of any descattering algorithm: the ideal descattering algorithm will allow density reconstructions on par with those from data with no scatter, and an algorithm that cannot improve over reconstructions from radiographs with scatter is not worth using at all. We apply the reconstruction methods described in Section IV to each of the direct fields, \mathbf{d}_t , and total fields, $\mathbf{d}_t + \mathbf{s}_t$, in the monoenergetic and polyenergetic testing sets. Because our datasets were generated via MCNP simulations, while our reconstruction algorithms use an analytical formulation, we expect a slight mismatch between the ground truth and reconstruction even when reconstructing in the no scatter case. We quantify the reconstruction errors in terms of the median absolute density error on the central slice of the 3D reconstruction,

$$\text{median}_{m,n} (|\hat{\rho}_t[m, n, 0] - \rho_t[m, n, 0]|), \quad (27)$$

in g/cm^3 , where $\hat{\rho}$ is the reconstructed density, ρ_t is the ground truth, and we let m and n range only over the area where $\rho_t[m, n, 0]$ is nonzero. (Recall that the objects we are imaging are 3D, hence the three indices for ρ .) We use the median rather than the mean because the mean is dominated by errors at the edge of the simulation and at the interface between materials. We believe these difference come from a slight geometric mismatch between the simulations and reconstruction geometry and are not addressed in this work.

Results for density reconstruction without descattering (Figure 4) show that the presence of scatter negatively impacts the accuracy of density reconstruction for both datasets, resulting in typical errors of over 0.5 g/cm^3 . In the polyenergetic dataset, there are errors of around 0.25 g/cm^3 even without scatter; we suspect these result from slight differences between the physical constants (beam spectrum and attenuation coefficients) between data generation and reconstruction. Looking at a representative reconstruction (Figure 3, right panel), we see

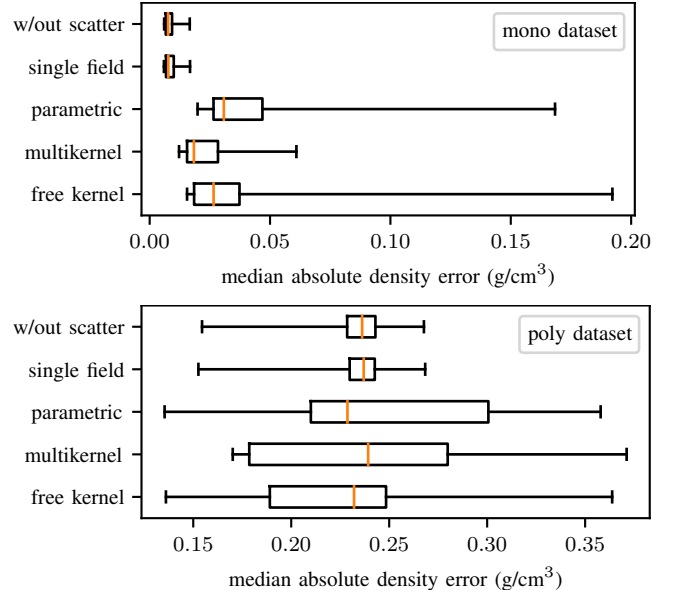


Fig. 5: Error in density reconstruction after oracle scatter fitting.

that the error due to scatter varies over the profile and can take the form of both density undershoots and overshoots.

E. Oracle Scatter Fitting

A scatter model's performance will be upper bounded by its ability to map from a single direct radiograph, \mathbf{d} to its corresponding scatter, \mathbf{s} , when both \mathbf{d} and \mathbf{s} are known. We would expect more complex models to perform better than simple ones at this fitting task; however, it does not give a complete picture of a model's potential for descattering, since, in practice, the true underlying \mathbf{s} is not known.

For each $(\mathbf{d}_t, \mathbf{s}_t)$ in the monoenergetic and polyenergetic testing sets, we fit a **single field**, **free kernel**, **parametric kernel** and **multi kernel** model with three kernels. (This is equivalent to performing local fitting with a single neighbor if the training set includes the testing set.) We use each fitted model to make a prediction, $\hat{\mathbf{s}}_t$. While we could evaluate the accuracy of scatter fitting by comparing the $\hat{\mathbf{s}}_t$'s and \mathbf{s}_t 's, this can be misleading for two reasons: first, errors in scatter estimation are much more consequential in regions where $\mathbf{d}[m, n]$ is small relative to $\mathbf{s}[m, n]$; second, because of the exponential relationship between areal mass and the measured signal (recall (3) and (5)), errors in the transmission domain propagate back to the density domain in unintuitive ways. To avoid these problems, We form an estimated direct transmission, $\hat{\mathbf{d}}_t = \mathbf{d}_t + \mathbf{s}_t - \hat{\mathbf{s}}_t$, and reconstruct, yielding $\hat{\rho}_t$. We compare these estimated densities to the ground truth in terms of median absolute density error (27).

The scatter fitting results (Figure 5) show that all models have some potential to improve density reconstruction via descattering, giving maximum density errors of under 0.2 g/cm^3 and 0.4 g/cm^3 in the monoenergetic and polyenergetic cases, respectively, as compared to errors of over 1.25 g/cm^3 when scatter is simply ignored (Figure 4). The single field model performs nearly identically to reconstruction without

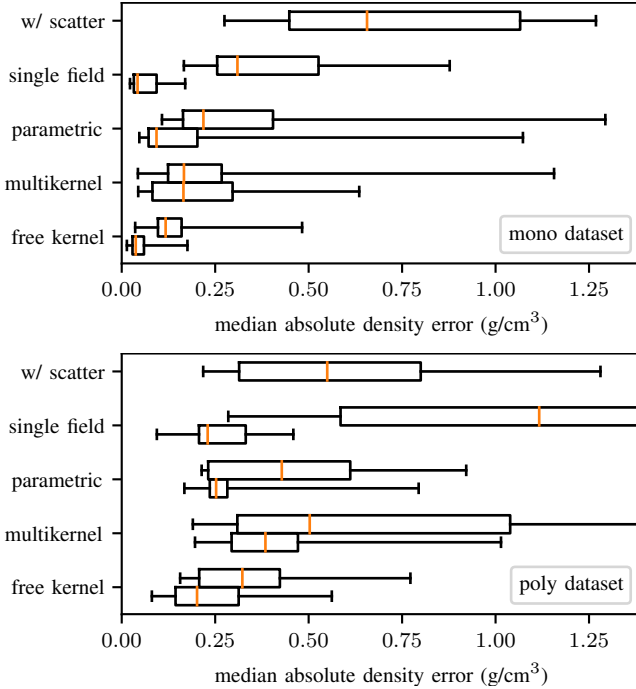


Fig. 6: Error in density reconstruction when scatter models are fit on training data and scatter is estimated from the direct radiograph and removed. Upper boxes: global model; lower boxes: local model. Local models provide significantly lower error.

scatter; this is expected, because each \hat{s}_t and s_t are identical except for the fact that, as described in Section V-B, we downsample by a factor of four during scatter fitting. It might be surprising that some models (in the polyenergetic) outperform reconstruction without scatter for some images. However, as we discussed in Section V-D, there is a slight mismatch between our forward simulations and the analytical reconstruction. For this reason, slight errors in \hat{d} may improve reconstruction by happenstance, e.g., by smoothing edges.

F. Scatter Estimation from Training Data

Next, we evaluate the methods in terms of scatter estimation, i.e., fitting on a training set and predicting the corresponding s for a (as yet unseen) d from the testing set. This experiment assumes d is known and evaluates only scatter estimation, rather than descattering performance. For the global version of the models, this means performing fitting as described in Section III-B on the entire training set (in our notation, $\mathbb{X} = 1, 2, \dots, T$); for the local models, the fitting is performed in the neighborhood of the new d ($\mathbb{X} = \mathbb{U}(d)$). In both cases, the resulting models are evaluated at the point d to estimate s . This experiment evaluates the generalization capability of each model, but it is still unrealistic in the sense that it presumes access to the direct transmission, d , whereas, in a descattering setting, we only have access to $t = d + s$, necessitating a descattering algorithm as described in Section III-C.

For each model, we compare the **global** version and the **local** version. For this and the subsequent experiments, we fixed the number of neighbors to two (we explore the effect

of the number of neighbors in Section V-I). Just as in the previous experiment, we compare results by estimating d and performing density reconstruction.

Results of the scatter estimation experiment (Figure 6) show that local modeling is superior to global modeling across all the models we compared and that excellent density errors can be achieved on both data sets. For example, the local free kernel model can reduce median density errors from 0.656 g/cm^3 to 0.038 g/cm^3 in the monoenergetic case and from 0.550 g/cm^3 to 0.202 g/cm^3 in the polyenergetic case. We plot representative estimated scatter profiles in Figure 7. While no model exactly matches the shape of the scatter, all four local versions get significantly closer than their global counterparts. We compare the kernel learned by the local free kernel method using the neighbors of a single profile to the global free kernel in Figure 8. While the two kernels have the same general shape, the global kernel is smoother than the local one, and they have a different scaling; this concurs with the results in Figure 7, where the local results tend to be sharper and better scaled with respect to the ground truth.

G. Full Descattering and Density Reconstruction

Our main experiment evaluates the ability of each of the models to enable accurate descattering and density reconstruction. The experimental setup mimics our actual application, i.e., we have access to a training set of (d_t, s_t) pairs, on which we fit scatter models. We are then given a new total radiograph, which we descatter via Algorithm 1. Finally, we reconstruct the underlying density based on the estimated direct radiograph and quantify the error using the median absolute density error (27).

The results for the descattering experiment (Figure 9) show that local models uniformly outperform global ones and that all of the descattering methods improve reconstruction accuracy over reconstructions without scatter removal, except for the global single field model on the polyenergetic dataset. These results are very similar to those in the scatter estimation (from known d) experiment in Section V-F, which suggests that, for our datasets, descattering performance is limited by scatter estimation performance. We show representative error profiles in Figure 10 and an error image for the free kernel method in Figure 11.

Convergence. We quantified the convergence of the fixed point algorithm by computing the normalized mean squared error (NMSE) at each iteration,

$$\|d + \hat{s}_d(d) - t\|_2^2 / \|t\|_2^2. \quad (28)$$

We plot a few representative convergence curves in Figure 12. Although the value of the NMSE and its rate of decrease varied from image to image, it would generally either plateau within a few iterations or drop to very low values (below 10^{-10}). In the latter case, this suggests that the fixed point algorithm finds a d such that $d + \hat{s}_d(d) = t$; in the former case, we suspect there is no solution to the system and we get $d + \hat{s}_d(d) \approx t$. This behavior occurred for both local and global models.

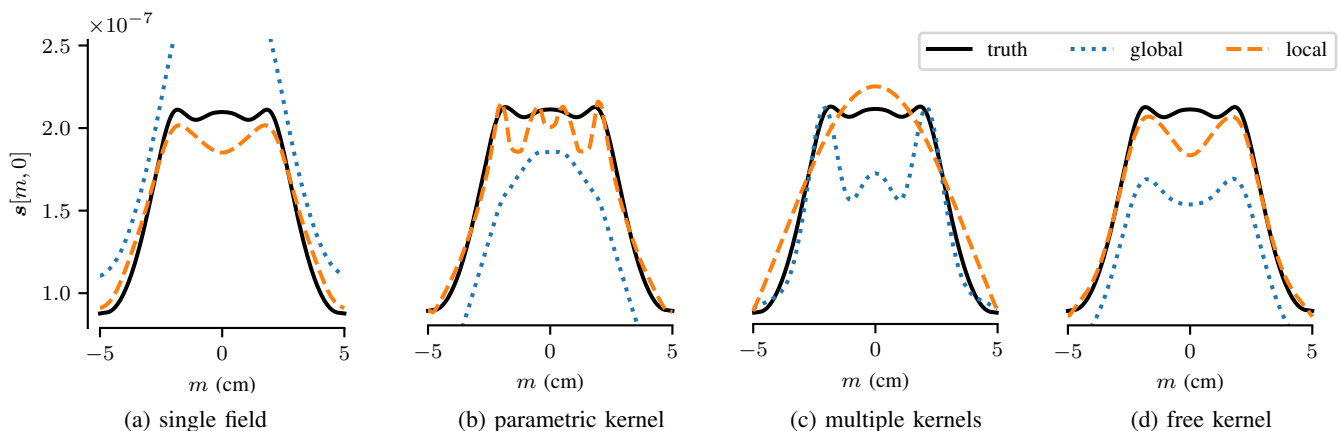


Fig. 7: Example scatter estimations from direct on the monoenergetic dataset, where fitting was performed on a separate training set.

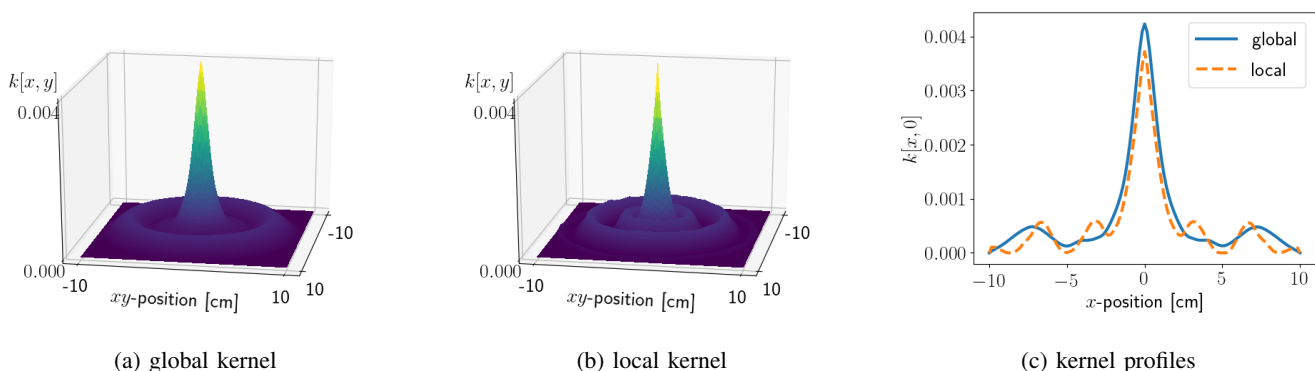


Fig. 8: Qualitative comparison of the global kernel versus the local kernel learned for a single profile, plotted here as a function of position in pixels. The local kernels tend to be sharper and give significantly more accurate scatter fits (see Figure 6).

H. Cases with Increased Scatter

To investigate the performance of local descattering as the amount of scatter increases, we chose a single object from the polyenergetic dataset and repeated the MCNP simulation with its mass scaled by a factor of 1.5 and 2 (leaving the collimator unchanged). These scaled objects have a much higher scatter-to-direct ratio than the original set, with a maximum ratio of 1.57 and 25.60, respectively, compared to 0.34 in the original dataset (where the maximum is computed over pixels).

For each of these scaled simulations, we additionally perturbed the density by adding or subtracting 1.0 or 2.0 g/cm^3 from the density of each shell, creating four variations. We fit a free kernel to these four variations and used it to descatter the scaled total transmission radiograph. Thus, we can think of the four variations as forming a local training set. We compare the original descattering result to the two high-scatter cases in Figure 13. The first trend we note is that, as the density increases, the reconstruction from the total radiograph (no descattering) deviates more and more from the ground truth, indicating that scatter has become a larger source of error. While descattering is successful in the original simulation and in the $1.5\times$ case, it begins to struggle in the $2\times$ case, reaching density errors of over 10 g/cm^3 in some regions. However, the local approach is still clearly better than ignoring scatter

altogether.

I. Effect of Number of Neighbors on Reconstruction Performance

We have, so far kept, the number of neighbors for the local models fixed at two. To evaluate the effect of the number of neighbors, we repeated the descattering experiment with the local free kernel model with the number of neighbors varying from one to five. The results (Figure 14) show that the reconstruction error is robust with respect to the number of neighbors, with local fitting consistently outperforming global no matter the number of neighbors. Although we might expect that a small number of neighbors could lead to overfitting and that increasing the number of neighbors may cause underfitting, we do not see clear evidence of this here. (Except that the global model, which is equivalent on our data to a local model with 90 neighbors, performs worse than the local ones.)

VI. DISCUSSION

While the parametric and multikernel models come from the literature and were derived based on physical principles, we chose the single field and free kernel models from a

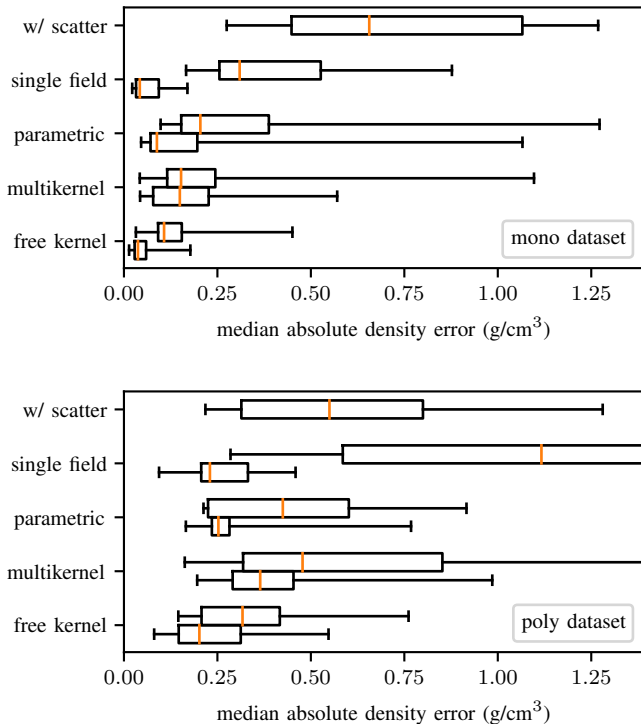


Fig. 9: Error in density reconstruction after descattering. The top box gives the error when scatter is not removed for sake of comparison. Upper boxes: global model; lower boxes: local model. In most cases, performing descattering was superior to leaving the scatter, and the local methods always outperformed their global counterparts.

purely function interpolation perspective; these warrant further discussion.

The single field model, fit on one neighbor, is equivalent to a nearest neighbor interpolator, i.e., $\mathcal{A}\{x\} \approx x_0$. A natural next step (in terms of complexity) is a linear interpolator, $\mathcal{A}\{x\} \approx Ax$. The problem here is that the matrix A is larger (the number of pixels in x squared) and very underdetermined, in the sense that a given x and y can be related by an infinite number of matrices A .

Restricting A to be a convolution does not reduce its expressive power very much: for any two vectors, x and y we can always find a kernel, k , such that $y = k * x$ whenever y 's support in the Fourier domain is a subset of x 's. This will occur when s is smoother than d , which makes physical sense. However, kernels fit in this manner will be unstable in the sense that the kernel may change rapidly with small changes in x and y ; this is undesirable because we want our models to generalize well to nearby (x, y) pairs.

Our proposed model is slightly more restrictive than a general convolutional model, because it requires the kernels to be nonnegative. It is not always possible to relate two signals via convolution with a nonnegative kernel, even when both signals are nonnegative. As a simple example, consider $x = [1/2 \ 1]^T$ and $y = [0 \ 1]^T$. The unique kernel that maps between them is $k = [4/3 \ -2/3]^T$, which has a

negative element. We can think of the nonnegativity constraint as providing a small amount of regularization that prevents the kernel from overfitting the training data. And, in practice, we do not use only one neighbor, providing some additional smoothing or regularization.

Taking a broader perspective, the local convolutional model is a piecewise linear function from images to images, i.e., $\mathbb{R}^{N_1 \times N_2} \rightarrow \mathbb{R}^{N_1 \times N_2}$. The pieces over which it is linear are defined by the neighborhoods in the training data. When the number of neighbors is one, these neighborhoods correspond exactly to Voronoi cells. When the number of neighbors is greater than one, the neighborhoods are higher order Voronoi cells. One could imagine fitting the entire model at training time, i.e., identifying all neighborhoods and performing model fitting in all of them. This would offer a speedup at model evaluation time (because fitting would already be complete) but doing so would require computing a large number of models, because the number of cells may be very large. Viewed this way, we can see that the local convolutional model is connected with convolutional neural networks (CNNs), which have proved to be powerful image-to-image regressors [25] and also have the form of a piecewise linear function [26]. Yet, they differ in the parameterization of the linear pieces and their boundaries.

Limitations. We now list a few limitations of the present study. Our simulations did not account for scatter within the detector, which depending on the hardware, may be nontrivial. Our local fitting method may be able to account for this type of scatter, but it would need to be included in the training data. Our testing datasets, although not small by the standards of other descattering work, are probably not large enough to detect small differences between methods, especially given the large amount of variation in the data.

VII. CONCLUSIONS AND FUTURE WORK

Taken together, our experiments show that modeling scatter locally is a useful approach both for scatter estimation and for descattering and density reconstruction. Of the four models we compared, we recommend the free kernel model, given that it is easy to fit and provides excellent descattering performance.

We see several possible extensions of this work. In the context of X-ray CT, our method should easily extend to multiview (i.e., not spherically symmetric) tomography problems, including medical imaging; however, these problems may necessitate gathering a larger training set. We would also like to study the effect of training set density on reconstruction performance; ideally, we could find a rule of thumb for how many simulations are needed to achieve a certain accuracy for a given application. Another direction may be to study different distance metrics for neighbor determination, or even to learn a good metric from the training data. Finally, we believe that the local modeling approach may have applications outside of scatter estimation. Wherever we have a training set of image pairs, we can potentially fit simple, instance-adaptive local models instead of complex, global models.

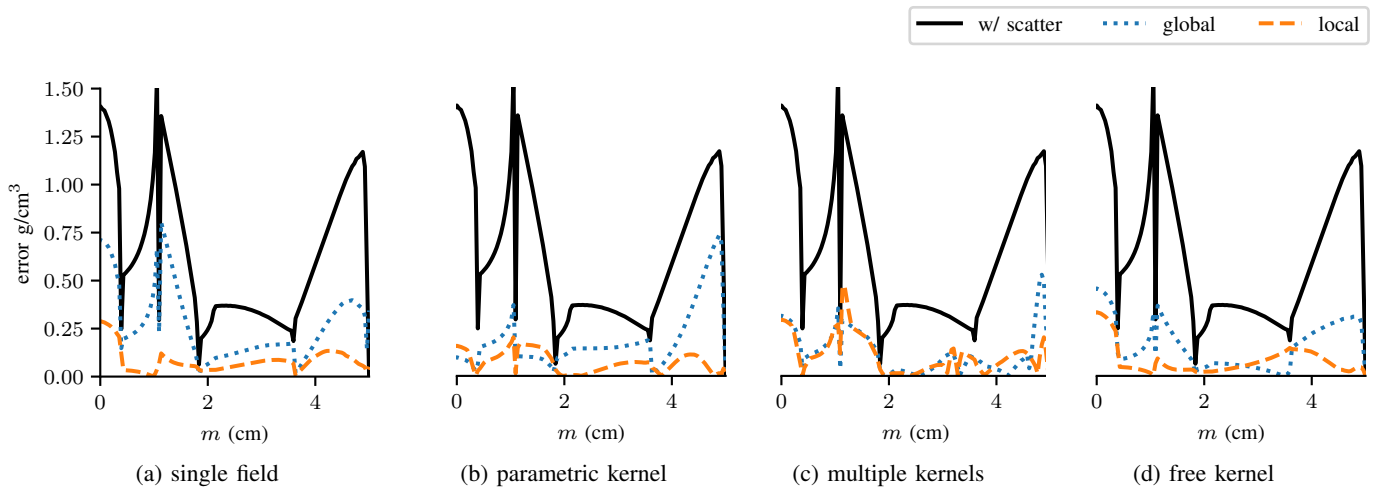


Fig. 10: Example reconstruction error profiles (monoenergetic dataset). Descattering improves density reconstruction across the entire profile and local models outperform their global counterparts for each model type.

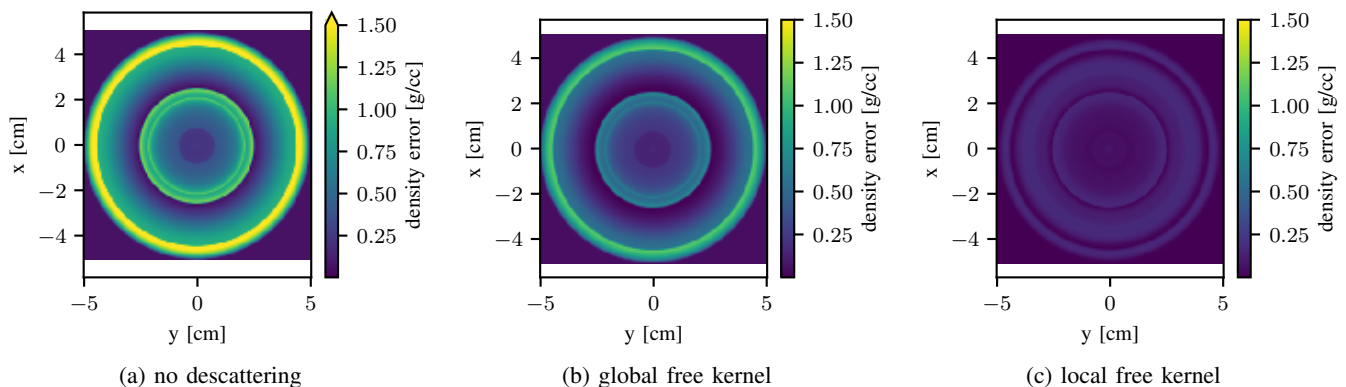


Fig. 11: Error magnitude in density reconstruction after descattering for one representative case in the polyenergetic dataset. The upward arrow in the colorbar in plot (a) indicates the presence of values above 1.50 g/cm^3 .

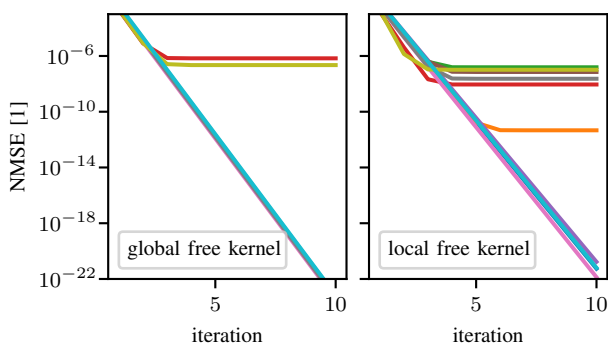


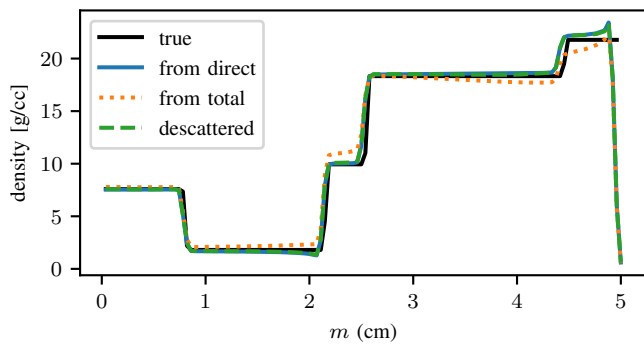
Fig. 12: Convergence of the fixed point algorithm (Algorithm 1) for the free kernel method on the monoenergetic dataset. Each line represents one image in the test set.

ACKNOWLEDGMENT

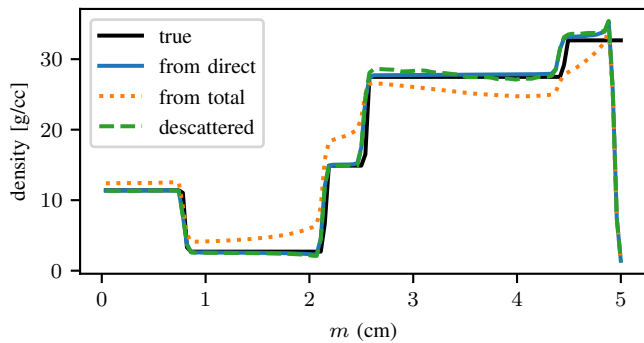
We thank Erik Skau, Luke Hovey, Brendt Wohlberg, and Alexander Sietsema.

REFERENCES

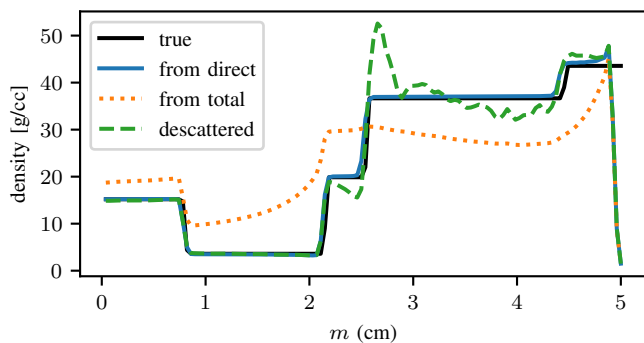
- [1] S. Ravishankar, J. C. Ye, and J. A. Fessler, "Image reconstruction: From sparsity to data-adaptive methods and machine learning," *Proceedings of the IEEE*, vol. 108, no. 1, pp. 86–109, Jan. 2020.
- [2] J. H. Mason, A. Perelli, W. H. Nailon, and M. E. Davies, "Polyquant CT: direct electron and mass density reconstruction from a single polyenergetic source," *Physics in Medicine & Biology*, vol. 62, no. 22, pp. 8739–8762, Nov. 2017.
- [3] I. Elbakri and J. Fessler, "Statistical image reconstruction for polyenergetic X-ray computed tomography," *IEEE Transactions on Medical Imaging*, vol. 21, no. 2, pp. 89–99, 2002.
- [4] C. Cohen-Tannoudji, J. Dupont-Roc, and G. Grynberg, *Atom-Photon Interactions: Basic Processes and Applications*. VCH PUBLN, 1998.
- [5] M. Sun and J. M. Star-Lack, "Improved scatter correction using adaptive scatter kernel superposition," *Physics in Medicine and Biology*, vol. 55, no. 22, pp. 6695–6720, Oct. 2010.
- [6] J. P. Stonestrom and A. Macovski, "Scatter considerations in fan beam computerized tomographic systems," *IEEE Transactions on Nuclear Science*, vol. 23, no. 5, pp. 1453–1458, 1976.
- [7] E.-P. Rührschopf and K. Klingenbeck, "A general framework and review of scatter correction methods in X-ray cone-beam computerized tomography. part 1: Scatter compensation approaches," *Medical Physics*, vol. 38, no. 7, pp. 4296–4311, Jun. 2011.
- [8] E.-P. Rührschopf, , and K. Klingenbeck, "A general framework and review of scatter correction methods in cone beam CT. part 2: Scatter estimation approaches," *Medical Physics*, vol. 38, no. 9, pp. 5186–5199, Aug. 2011.
- [9] B. Ohnesorge, T. Flohr, and K. Klingenbeck-Regn, "Efficient object scatter correction algorithm for third and fourth generation CT scanners," *European Radiology*, vol. 9, no. 3, pp. 563–569, Mar. 1999.
- [10] J. Maier, S. Sawall, M. Knaup, and M. Kachelrieß, "Deep scatter estimation (DSE): Accurate real-time scatter estimation for X-ray CT



(a) original simulation



(b) 1.5× density



(c) 2× density

Fig. 13: Effect of increasing object density on descattering performance using a local free kernel model and fixed-point descattering (Algorithm 1). As the density scales up, the scatter-to-direct ratio increases, making descattering and reconstruction more challenging.

using a deep convolutional neural network,” *Journal of Nondestructive Evaluation*, vol. 37, no. 3, Jul. 2018.

- [11] D. Tisseur, N. Bhatia, N. Estre, L. Berge, D. Eck, and E. Payan, “Evaluation of a scattering correction method for high energy tomography,” *EPJ Web of Conferences*, vol. 170, p. 06006, 2018.
- [12] A. Kak and M. Slaney, *Principles of Computerized Tomographic Imaging*, ser. Classics in Applied Mathematics. New York, NY: Society for Industrial and Applied Mathematics, 2001.
- [13] M. Berger *et al.* Xcom: Photon cross section database (version 1.5). [Online]. Available: <http://physics.nist.gov/xcom>
- [14] C. J. Werner *et al.*, “MCNP version 6.2 release notes.” Los Alamos National Laboratory, Tech. Rep. LA-UR-18-20808, 2018.
- [15] S. Agostinelli *et al.*, “Geant4—a simulation toolkit,” *Nuclear Instru-*

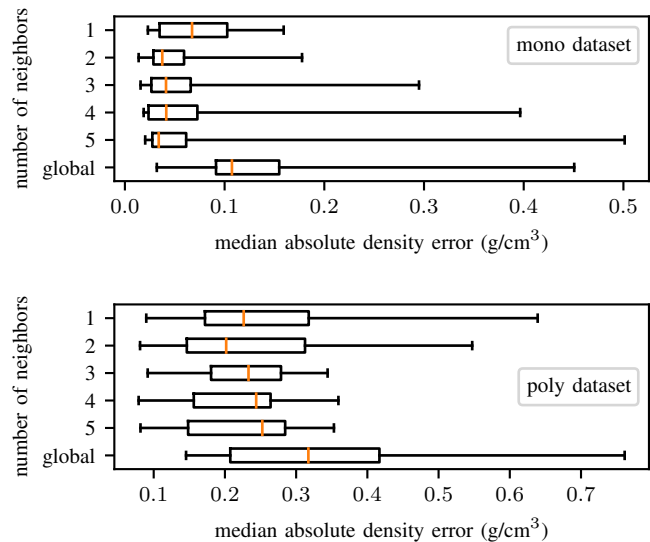


Fig. 14: Effect of the neighborhood size on density reconstruction error using the local free kernel.

ments and Methods in Physics Research Section A: Accelerators, Spectrometers, Detectors and Associated Equipment, vol. 506, no. 3, pp. 250–303, Jul. 2003.

- [16] D. Chen and R. J. Plemmons, “Nonnegativity constraints in numerical analysis,” in *A. Bultheel and R. Cools (Eds.), Symposium on the Birth of Numerical Analysis*, World Scientific. Press, 2009.
- [17] J. Cantarella and M. Piatek, “Tsnlns: A solver for large sparse least squares problems with non-negative variables,” *arXiv*, 2004.
- [18] S. Boyd, N. Parikh, E. Chu, B. Peleato, and J. Eckstein, “Distributed optimization and statistical learning via the alternating direction method of multipliers,” *Foundations and Trends in Machine Learning*, vol. 3, no. 1, pp. 1–122, Jan. 2011.
- [19] J. Shewchuk, “An introduction to the conjugate gradient method without the agonizing pain,” Carnegie Mellon University, Tech. Rep., 1994.
- [20] D. C. Liu and J. Nocedal, “On the limited memory BFGS method for large scale optimization,” *Mathematical Programming*, vol. 45, no. 1-3, pp. 503–528, aug 1989.
- [21] M. T. McCann and M. Unser, “Biomedical image reconstruction: From the foundations to deep neural networks,” *Foundations and Trends in Signal Processing*, vol. 13, no. 3, pp. 283–359, Dec. 2019.
- [22] C. J. Dasch, “One-dimensional tomography: a comparison of abel, onion-peeling, and filtered backprojection methods,” *Applied Optics*, vol. 31, no. 8, p. 1146, mar 1992.
- [23] M. Beister, D. Kolditz, and W. A. Kalender, “Iterative reconstruction methods in X-ray CT,” *Physica Medica*, vol. 28, no. 2, pp. 94–108, Apr. 2012.
- [24] T. Oliphant, “NumPy: A guide to NumPy,” USA: Trelgol Publishing, 2006. [Online]. Available: <http://www.numpy.org/>
- [25] M. T. McCann, K. H. Jin, and M. Unser, “Convolutional neural networks for inverse problems in imaging: A review,” *IEEE Signal Processing Magazine*, vol. 34, no. 6, pp. 85–95, Nov. 2017.
- [26] G. F. Montufar, R. Pascanu, K. Cho, and Y. Bengio, “On the number of linear regions of deep neural networks,” in *Advances in Neural Information Processing Systems*, Z. Ghahramani, M. Welling, C. Cortes, N. Lawrence, and K. Q. Weinberger, Eds., vol. 27. Curran Associates, Inc., 2014, pp. 2924–2932.